Differential diffusion effects in counter-flow premixed hydrogen-enriched methane and propane flames

Ehsan Abbasi-Atibeh[a], Jeffrey M. Bergthorson[a,*]

[a]*Department of Mechanical Engineering, McGill University, Montreal, QC H3A 0C3, Canada*

Abstract

The effects of differential diffusion and stretch sensitivity on propagation and stabilization of lean premixed hydrogen-enriched methane-air and propane-air flames are studied in a turbulent counter-flow apparatus. In these experiments, the unstretched laminar flame speed is kept constant through decreasing the mixture equivalence ratio, in order to minimize the effects of chemistry and highlight the effects of differential diffusion during hydrogen-enrichment. Bulk flow properties are also kept constant between laminar and turbulent flames. High-speed Particle Image Velocimetry (PIV) is applied to quantify the flow velocity field using oil droplet seeding, enabling simultaneous flame position and velocity measurements. Data processing tools are developed through this study to quantify instantaneous local measurements of flame position, flame curvature, and apparent turbulent flame velocity within the imaged plane. Probability Density Functions (PDFs) of instantaneous flame position showed that, in hydrogen-enriched methane-air flames (effective Lewis number < 1), differential diffusion increases the turbulent burning rates throughout the whole hydrogen-enrichment range. However, in hydrogen-enriched propane-air flames, these effects are only observed at hydrogen content above 60 % (by volume), where effective Lewis number falls below unity. PDFs of flame position also illustrated that the effects of differential diffusion become significant when the effective Lewis number < 0.8. In contrast, PDFs of turbulent flame velocities only showed a slight increase in local instantaneous velocities with increasing hydrogen content. Furthermore, it was illustrated that differential diffusion affects the flame front topology by increasing instantaneous flamelet curvature at below unity Lewis numbers, consistent with flame stability theory.

Keywords:
Differential diffusion, Hydrogen-enrichment, Turbulent premixed combustion, Particle Image Velocimetry (PIV)

*Corresponding author:
Email address: jeff.bergthorson@mcgill.ca (Jeffrey M. Bergthorson)

1. Introduction

Fuel-flexibility of newly-designed engines is an important parameter of combustor performance due to increasing demand for renewable alternative fuels, and also energy security concerns. However, turbulent combustion of mixtures with different chemistry and transport properties brings large uncertainty in the design of fuel-flexible combustors, mainly due to variations in turbulent burning rates, which significantly affect combustor operability issues, such as blow out, flash back, and dynamic stability.

Changing the fuel composition has two major impacts on flame propagation: 1) it changes the chemical properties of the mixture, which increases the flame velocity with increasing H_2 content in laminar hydrocarbon flames [1, 2], and 2) it changes the transport properties (diffusivity of deficient species and heat), which plays an important role in the propagation of premixed flames [3–8], and is known as "differential diffusion".

Differential diffusion effects on the propagation of premixed flames are coupled with stretch sensitivity at the flame front. Stretch rate (K), is defined as the normalized differential change in flame surface area as a function of time: $K = (1/A)/(\mathrm{d}A/\mathrm{d}t)$, and can be expressed as a function of flame curvature (κ) and hydrodynamic strain (K_s) [9]: $K = S_L\kappa + K_s$. The effects of stretch are highly important in the propagation of premixed flames, which have been studied in detail for laminar flames [10, 11], and for turbulent flames [12, 13]. Lewis number (Le), defined as: $\mathrm{Le} = \alpha/\mathcal{D}$, determines the relative role of heat and mass diffusion (thermo-diffusive properties) at the flame front, and controls the stretch sensitivity of premixed flames.

In this study, the effects of differential diffusion on propagation and stabilization of highly-stretched H_2-enriched CH_4-air and C_3H_8-air flames are studied. H_2-enrichment at various volume ratios forms mixtures with different fuel diffusivity illustrative of distinct Le.

H_2-enriched flames have been investigated in a number of studies [14, 15]; however, in the majority of these studies, chemical effects are not isolated from differential diffusion effects. Furthermore, turbulent flame velocity measurements reported in the majority of studies are focused on global time-averaged measurements, that do not necessarily yield local information on the physics of turbulent flame propagation [16].

Therefore, in this study, the effects of differential diffusion are highlighted by keeping the unstretched laminar flame speed (S_L^o) constant during H_2-enrichment. Furthermore, instantaneous local measurements of apparent flame position and turbulent flame velocity components within the imaged plain are used to study differential diffusion effects at constant bulk flow properties in a hot exhaust counter-flow rig.

2. Experimental method

Experiments in this study investigate lean premixed turbulent and laminar combustion of H_2-enriched CH_4-air and C_3H_8-air flames under atmospheric pressure. A CH_4-air flame at $\phi = 0.7$ and a C_3H_8-air flame at $\phi = 0.659$ are selected as reference mixtures, both having a predicted $S_L^o = 0.195$ m/s. During the enrichment process, H_2 is added to reference mixtures in increments of 10 % (by volume), while S_L^o is kept constant at 0.195 m/s, through decreasing the mixture equivalence ratio (ϕ). The bulk flow velocity at the nozzle exit (U_{out}) is also kept constant in all experiments at 4.5 m/s. Properties of these mixtures are listed in Table 1. Keeping S_L^o constant minimizes the effects of chemical properties of the mixture on the propagation and stabilization of premixed flames, and highlights the effects of differential diffusion, in order to study the effects of thermo-diffusive properties of the fuel in fuel-flexibility experiments. H_2 content in turbulent flame experiments was increased up to the flash-back limit of 70 % and 90 % for CH_4-H_2-air and C_3H_8-H_2-air flames, respectively.

Lewis number is defined as: $\mathrm{Le} = \alpha/\mathcal{D} = \lambda/(\rho c_p \mathcal{D})$, and is calculated at room temperature and pressure of 300 K and 1 atm, respectively. λ is the thermal conductivity, c_p is specific heat, ρ is the density of the unburned reactants, and $\mathcal{D}$ is the fuel diffusivity. The effective Le is defined based on volumetric fraction-weighted average formulation [17]: $\mathrm{Le_{eff}} = X_{C_nH_m}\mathrm{Le}_{C_nH_m} + X_{H_2}\mathrm{Le}_{H_2}$, where X is the mole fraction in the fuel stream. As listed in Table 1, $\mathrm{Le_{eff}}$ decreases with increasing H_2 content in the fuel stream from 0.97 for CH_4-air, and from 1.86 for C_3H_8-air, down to 0.376 for pure H_2.

Diffusive flame thickness ($\delta_L = \lambda/(c_p \rho_u S_L^o)$), and adiabatic flame temperature (T_{ad}) are calculated using free-flame simulations in Cantera [18], and listed in Table 1. GRI-Mech 3.0 and AramcoMech 1.3 reaction mechanisms are used for computations involving CH_4 and C_3H_8, respectively.

2.1. Hot exhaust opposed-flow turbulent flame rig

Experiments are conducted in a Hot exhaust Opposed-flow Turbulent Flame Rig (HOTFR) [19–25]. The rig is designed to stabilize turbulent flames against a hot product flow in an axial counter-flow configuration. In HOTFR, the flow from the premixed fuel and air nozzle at the bottom impinges against hot products

H_2 [%]	CH_4+H_2+air				C_3H_8+H_2+air			
(by Vol.)	ϕ	Le_{eff}	δ_L [mm]	T_{ad} [K]	ϕ	Le_{eff}	δ_L [mm]	T_{ad} [K]
0	0.7	0.97	0.271	1842	0.659	1.86	0.248	1817
20	0.668	0.85	0.280	1800	0.647	1.56	0.252	1799
40	0.628	0.73	0.291	1746	0.630	1.27	0.259	1774
60	0.578	0.61	0.306	1679	0.602	0.97	0.270	1733
80	0.513	0.50	0.327	1593	0.547	0.67	0.291	1650
100	0.423	0.38	0.363	1481	0.423	0.38	0.363	1481

Table 1: Properties of CH_4+H_2+air and C_3H_8+H_2+air mixtures at S_L^o = 0.195 m/s.

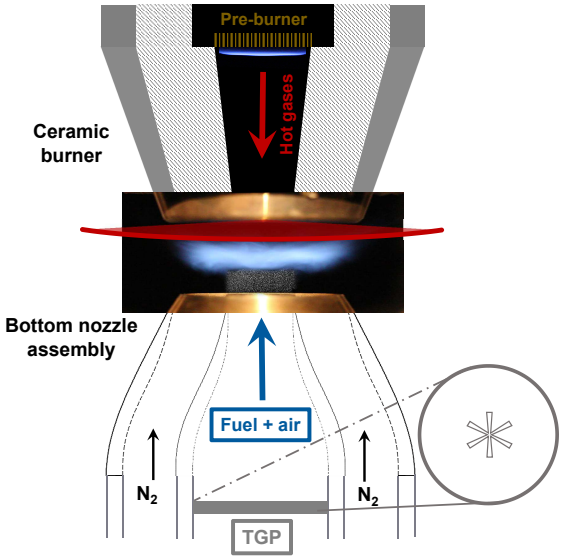

Figure 1: Schematic of HOTFR and S-TGP.

from a pre-burner inside the ceramic burner at the top. A co-flow of inert gas is used to reduce the effect of the shear layer, stabilize the flame edge, and shroud the opposed flow from surrounding air. The exit diameter of the premixed fuel and air nozzle (d_N) is 20 mm, and the separation distance between the two nozzles is 1.4 d_N. The schematic of HOTFR is shown in Fig. 1.

A CH_4-air mixture at ϕ = 0.75, and T_{ad} = 1924 K is used to feed the top nozzle, and the nozzle exit velocity ($U_{CB} \approx 13$ m/s) is kept constant in all experiments. The temperature of hot exhaust gases at the ceramic nozzle exit is measured using R-type thermocouples, and corrected for heat losses [8]: T_{CB} = 1837 K. Radial temperature profiles are fairly constant, and the repeatability of T_{CB} readings are verified through multiple measurements with an uncertainty of ~ 1 % of the reading.

Turbulence in the test area is generated using a Star-shaped high-blockage Turbulence Generating Plate (S-TGP) with an open area of 2.4 % [26], as illustrated in Fig. 1. Higher turbulence intensity assures combustion in the thin reaction zone of the Borghi diagram [27], and allows experiments closer to relevant conditions of Gas-Turbine Engines (GTE) and other combustors. S-TGP is removed in laminar flame experiments while flow conditions and mixture compositions are preserved.

In turbulent experiments, S-TGP distance from the nozzle exit (H) was set at H/D_P = 2.4. This distance was chosen to be larger than that found to minimize large-scale bulk-flow oscillations, as shown in [26] using energy spectra of S-TGP for various H. These large-scale oscillations are caused by vortex shedding from the TGP holes and are minimized by using a single-jet TGP design and increased H [28]. Furthermore, the contoured design of the nozzles is also effective in damping jet-wake interactions downstream of the TGP.

The rig has a compact geometry and excellent optical accessibility, where aerodynamically-stabilized lifted flames are not affected by conductive heat loss to the burner and are stabilized against a uniform flow of hot combustion products. Therefore, it provides clear boundary conditions and a compact experimental zone that reduces the complexity and makes it ideal for validating Computational Fluid Dynamics (CFD) models.

2.2. Diagnostic method and processing techniques

2.2.1. Particle image velocimetry

The flow velocity field is quantified using Two-Dimensional high-speed Particle Image Velocimetry (2D-PIV) within the imaged plane. Atomized oil droplets ($\approx 1\,\mu$m) are seeded into the flow, through an atomizer, as tracer particles, and are illuminated using a Nd:YLF laser at 527 nm wavelength. The Mie scattered light is captured using a high-speed CMOS camera at imaging speed of 12 kfps. 10 000 PIV image pairs are post-processed using the DaVis PIV software package to calculate the two-component velocity vector field within the plane of the laser sheet at each turbulent run, whereas 500 images are used in each laminar experiment. The smallest interrogation window used in PIV calculations is a 16 × 16 pixel grid with a window overlap of 75 %. The pixel-to-mm ratio is 44.7, yielding a PIV spatial resolution of $\approx 358\,\mu$m, and a grid-spacing of $\approx 89.5\,\mu$m in these experiments.

H_2 [%] (by Vol.)		$\overline{U}/S_L^o$	u'/S_L^o	u'/U	L/δ_L	L/η	Re_T	Ka_T	Da_T
CH_4+H_2+air	0	23.1	8.4	0.36	9.9	29.0	89.0	8.6	1.2
	70	21.6	7.3	0.34	10.0	28.2	85.9	8.0	1.4
C_3H_8+H_2+air	0	23.5	7.8	0.33	11.3	29.5	91.0	6.8	1.5
	90	21.8	7.4	0.34	10.3	28.9	88.5	7.9	1.4

Table 2: Experimental conditions of turbulent CH_4+H_2+air and C_3H_8+H_2+air flames at $S_L^o = 0.195$ m/s using S-TGP.

Turbulent flow statistics of the mean velocity ($\overline{U}$) and root-mean-square (rms) of velocity fluctuations (u' in axial direction and v' in radial direction) are calculated, and the results are listed in Table 2 for pure hydrocarbon flames and H_2-enriched flames near the flash-back region, where $\overline{U}$ and u' are averaged over the test domain at 0.7 mm above the nozzle exit, and upstream of the flame brush, respectively. PIV uncertainty in estimating the velocity vector field is calculated based on the velocity-lag of tracer particles due to Stokes-drag force, resulting in an uncertainty of less than 1 % in unburned gas mixture in turbulent flame experiments. Details of these calculations are discussed in [8].

The performance of the S-TGP in generating turbulence is illustrated in Fig. 2. u' and v' velocity profiles show that turbulence statistics in the test section is nearly isotropic ($u' \approx v'$), and axial turbulence intensity fluctuates slightly within the range of $31\,\% \leq u'/U \leq 36\,\%$, as listed in Table 2.

The integral length scale (L) is estimated using the autocorrelation function [29, 30]. An estimation for the ratio of largest to smallest hydrodynamic length scales in a turbulent flow can be derived as [29]: $L/\eta \approx Re_T^{3/4}$, where η is the Kolmogorov length scale, and Re_T is the turbulent Reynolds number: $Re_T = u'\,L/\nu$. Re_T is calculated upstream of the flame brush, in the preheat zone at $T \approx 576$ K, which is the flash point of oil used for seeding, whereas, the cold flow equivalent of Re_T is around 240. Studying turbulence-chemistry interactions in this range of Re_T is of specific interest in the validation of flamelet models, in the region where mixing and chemical time scales are comparable.

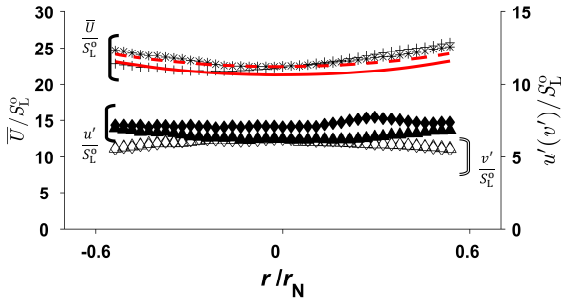

Figure 2: Nozzle exit u' (♦ and ▲), v' (◊ and △), turbulent $\overline{U}$ (+ and ∗), and laminar $\overline{U}$ (solid and dash) of CH_4+air and C_3H_8+air flames, respectively, in radial direction.

Turbulent Karlovitz number: $Ka_T = (L/\delta_L)^{-2}\ Re_T^{1.5}$, and turbulent Damköhler number: $Re_T = Da_T^2\ Ka_T^2$ [31] are listed in Table 2. Ka_T and Da_T are also calculated at $T \approx 576$ K. According to the experimental conditions listed in Table 2, these flames are located in the thin reaction zone of the Borghi diagram [27, 31].

2.2.2. *Processing techniques*

Mie scattering of light from atomized oil droplets allows simultaneous flame-position and velocity-field measurements [32, 33]. Atomized oil droplets seeded into the flow evaporate at the flame front and terminate the light scattering. Hence, the pixel light intensities from PIV images can be processed using flame surface tracking methods to track the flame front. In this technique, it is assumed that combustion occurs inside a relatively thin layer, and that the flamelet model [31] is valid. A sample PIV image is illustrated in Fig. 3 (a), showing the test domain at $-0.25 \leq (r/d_N) \leq 0.25$.

In flame-front tracking, an edge detection algorithm is applied to find positions of maximum pixel intensity gradient on a PIV image, and localize the edges, resulting in instantaneous flame front topology within the imaged flame. A quantized PIV image with the resulting flame front is shown in Fig. 3 (b). The main uncertainty sources of this method are the mean tracer particle distance, the oil droplet lifetime at the flame front, uncertainties imposed by filtering process during post processing, and oil droplet illumination in PIV images [8], resulting in a total uncertainty of less than $0.5\,\delta_L$.

The local turbulent flame displacement velocity (S_T) is the propagation velocity of the local flamelet (S_F) relative to the convection velocity of the flow (S_u) in the direction normal to the flame surface ($\vec{n}$) [16, 34–36]: $S_T = (S_F + S_u) \cdot \vec{n}$. S_T measurement is discussed in detail in the study of Trunk *et al.* [35]. However, in the current study, the 2D projection of S_T is measured using 2D-PIV and single-plane imaging, which is the apparent turbulent flame velocity within the imaged plane,

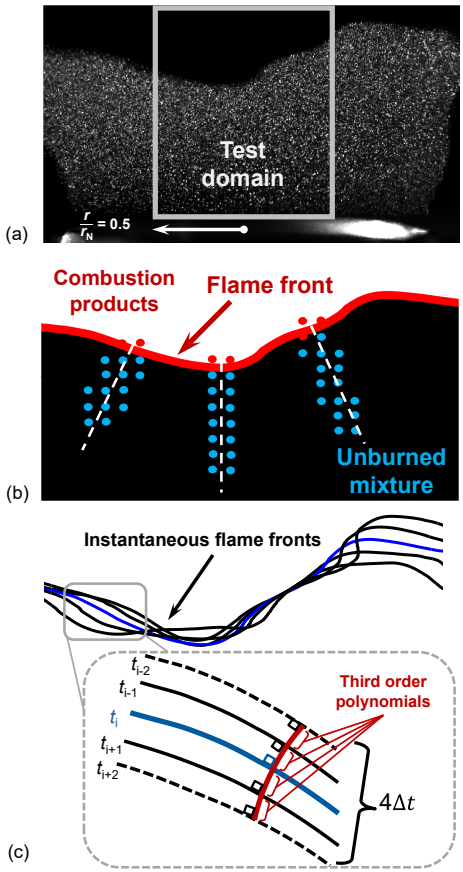

Figure 3: Processing techniques: (a) a sample PIV image indicating the test domain, (b) a quantized PIV image with a distinguished flame front illustrating the schematic of S_u measurement, and (c) 5 successive flame fronts and a schematic showing S_F calculation.

and is noted as S_T for simplicity.

Hartung *et al.* [36] showed that the 2D projection of S_T is, indeed, a sensitive parameter in turbulence-chemistry interactions, and that more complex 3D measurements might not result in significant extra information. The experiments have the advantage of relative simplicity and superior precision compared to complex 3D measurements, which present a suitable method for quantification of turbulence-chemistry interactions with a specific potential in the validation of CFD simulations. They also provide adequate data to address the effects of differential diffusion on flame propagation in the context of fuel-flexibility, which is the main focus of this study.

The instantaneous two-component unburned gas velocity upstream of the flame front (S_u) is calculated using the velocity grid network in the vicinity of the normal line, as seen in Fig. 3 (b). Due to a significant decrease in signal-to-noise ratio, and increased uncertainty in PIV velocity vectors within the regions of elevated temperatures in the preheat zone [35], a local velocity minimum at the edge of the preheat zone is considered as the most appropriate local convective velocity. However, in turbulent flames, this minimum is not always recognized due to the movement of the flame, and the average of the two closest velocity vectors to the flame is considered as S_u upstream of the flame front.

Axial hydrodynamic strain rate (K_s) is computed by a linear fitting to the projected velocity values in the unburned region along the normal line. These calculations are done within 1.5 mm upstream of the flame front (equivalent to 5-9 independent velocity data), over 10 000 PIV images to approach the PDF of K_s.

In order to measure instantaneous apparent flame front velocity (S_F), the flamelet's path between 5 consecutive flame fronts within the imaged plane is estimated using 4 continuous 3^{rd}-order polynomials to reconstruct the flame motion, which are perpendicular to all 5 flame fronts and the total length is a minimum [37]. A 4^{th}-order finite difference method is used to calculate displacement data for each segment of the flame, which is used in calculation of S_F. This method is illustrated schematically in Fig. 3 (c). S_F is considered positive when the velocity is toward the unburned gas, and is considered negative in the opposite direction.

In laminar flame experiments, the unburned gas velocity upstream of the flame front ($S_{u,ref}$) is measured as the minimum of the averaged velocity profile, along the nozzle centerline.

3. Results and discussion

PDFs of instantaneous flame position within the imaged plane (Z_f) at increasing H_2-enrichment are shown in Fig. 4 (a) and (b), where $Z_f = 0$ is located at the exit plane of the bottom nozzle. PDFs of Z_f give statistics of the flame location, and the range of flame movement. The expected flame location ($\langle Z_f \rangle$), as well as the flame brush thickness, $\delta_T = 4 \times \sigma$, where σ is the standard deviation of the PDFs, can be extracted. Furthermore, the skewness of the PDFs indicates a propensity for the flame location to be upstream or downstream of $\langle Z_f \rangle$.

As shown in Fig. 4 (a) and (b), PDFs of the pure hydrocarbon flames are skewed toward the stagnation surface, as they are pushed to the hot exhaust gases by steep average velocity gradients. In H_2-enriched flames, with increasing H_2-enrichment, PDFs of Z_f move toward the bottom nozzle and become less skewed, which shows that the enriched flames have a higher tendency to burn faster and climb up the velocity gradient toward the unburned mixture. This relocation is clearly seen in CH_4-H_2-air flames at H_2 content as low as 20 %, whereas in

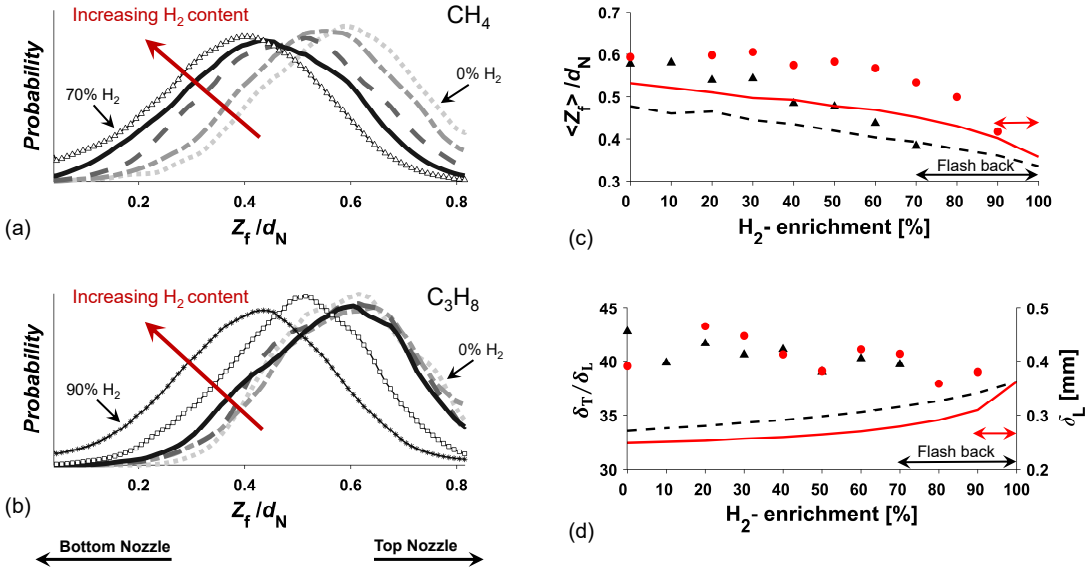

Figure 4: PDFs of Z_f for turbulent: (a) CH_4-H_2-air, and (b) C_3H_8-H_2-air flames at increasing H_2-enrichment of 0 % (dot), 20 % (dash-dot), 40 % (dash), 60 % (solid), 70 % (△), 80 % (□), and 90 % (∗). (c) $\langle Z_f \rangle$ of turbulent (symbol) and laminar (line): CH_4-H_2-air (▲ and dash), and C_3H_8-H_2-air (● and solid) flames, respectively. (d) δ_T of turbulent (symbol) and δ_L of laminar (line): CH_4-H_2-air (▲ and dash), and C_3H_8-H_2-air (● and solid) flames, respectively.

C_3H_8-H_2-air flames, PDFs of Z_f show a slight tendency to move toward the fresh reactants up to H_2 contents of 60 %, and a considerable movement toward the bottom nozzle at H_2 contents above 60 %.

In order to quantify these effects, $\langle Z_f \rangle$ of turbulent and laminar flames, as well as δ_T and δ_L variations, are summarized in Fig. 4 (c) and (d). Figure 4 (c) illustrates that highly-strained laminar flames also move further upstream toward the unburned reactants with increasing H_2 content. Cold flow experiments show that the momentum change in opposed-jet streams during the enrichment from 0 % to 100 %, results in a relocation of the stagnation surface of less than $0.02\,\langle Z_f \rangle / d_N$ toward the bottom nozzle. $\langle Z_f \rangle$ decreases linearly in CH_4-H_2-air flames, as Le_{eff} is also decreasing linearly from a value close to one to 0.38 for the pure H_2-air flame. In C_3H_8-H_2-air flames, in contrast, the slope appears to change after 70 % of H_2 content once differential diffusion effects become effective at $Le_{eff} < 1$. Similar behavior is observed in turbulent C_3H_8-H_2-air flames, where $\langle Z_f \rangle$ is almost constant up to H_2-enrichment of 60 %, and drops significantly after 70 % ($Le_{eff} \leq 0.82$), whereas, in CH_4-H_2-air flames, decreasing trend in $\langle Z_f \rangle$ is observed at H_2 content of as low as 20 %, and is more significant after 30 % ($Le_{eff} \leq 0.79$). Flash-back regions are illustrated in Fig. 4 (c) and (d) for turbulent flames.

Normalized δ_T (Fig. 4 (d)) is almost constant, while δ_L slightly increases with increasing H_2-enrichment at constant laminar flame speed.

PDFs of S_T are illustrated in Fig. 5 (a) and (b). The key features of these PDFs are the most probable apparent turbulent flame velocity ($\langle S_T \rangle$), and the distribution of PDFs compared to S_L^o. These PDFs include the velocity data up to 60 % and 80 % of enrichment for CH_4-H_2-air and C_3H_8-H_2-air flames, respectively, as extensive wrinkling of the enriched flames at distances too close to the nozzle exit, at the near flash-back limit, significantly decreases the signal-to-noise ratio in S_u, S_F, and S_T measurements.

As illustrated in Fig. 5 (a), PDF of S_T in CH_4-air flame shows values in the range of $-2 \lesssim S_T/S_L^o \lesssim 8$, consistent with local 3D turbulent displacement velocity measurements reported in [35], which further validates the current measurements. DNS study of 2D stoichiometric CH_4-air flames [38] also supports the existence of negative S_T values, in the highly curved regions.

PDFs of S_T in H_2-enriched CH_4-air flames move toward slightly higher velocities by increasing H_2 content. However, in C_3H_8-H_2-air flames, PDFs of S_T are not sensitive to the effects of differential diffusion at low H_2 contents, and start to move toward higher velocities at higher H_2 concentrations. PDFs of S_T are normally distributed and look almost similar for both flame mixtures.

$\langle S_T \rangle$ and $S_{u,ref}$ are plotted versus H_2 content in Fig. 5 (c). In general, $\langle S_T \rangle$ is larger than $S_{u,ref}$, due to the fact that turbulent flames also have local curvature to

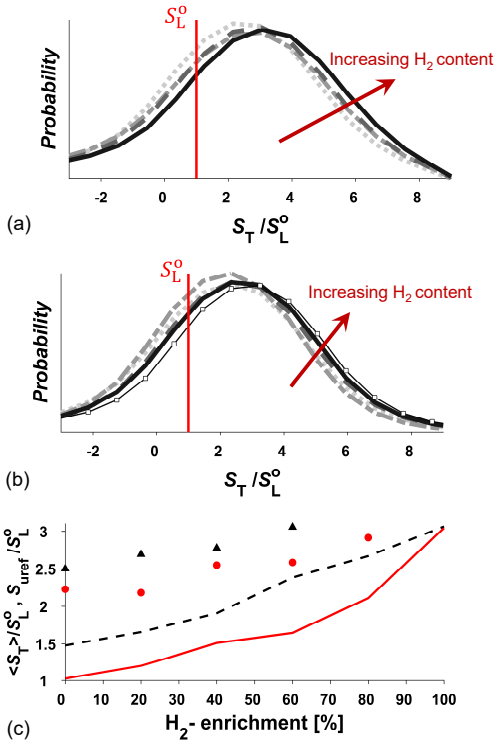

Figure 5: PDFs of S_T for turbulent: (a) CH_4-H_2-air, and (b) C_3H_8-H_2-air flames at increasing H_2-enrichment of 0 % (dot), 20 % (dash-dot), 40 % (dash), 60 % (solid), and 80 % (□). (c) S_T (▲ and ●) and $S_{u,ref}$ (dash and solid) correlations of CH_4-H_2-air and C_3H_8-H_2-air flames at increasing H_2-enrichment, respectively.

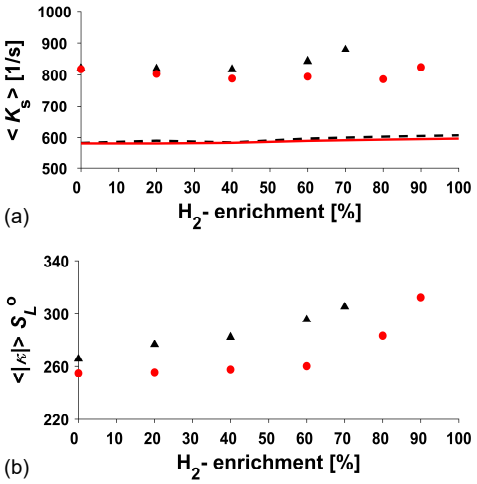

Figure 6: Components of flame stretch: (a) $\langle K_s \rangle$ of turbulent and laminar: CH_4-H_2-air (▲ and dash), and C_3H_8-H_2-air (● and solid) flames, (b) $\langle \kappa \rangle$ of CH_4-H_2-air (▲) and C_3H_8-H_2-air (●) turbulent flames, respectively.

enhance the local flamelet burning rate. In turbulent flames, $\langle S_T \rangle$ is 2 to 3 times larger than S_L^o, which indicates the propensity of these flames to burn faster when stretched, as also shown in [36].

As shown in Fig. 5 (c), $\langle S_T \rangle$ is larger in CH_4-H_2-air compared to C_3H_8-H_2-air flames, and it shows a slight increase with increasing H_2 content due to differential diffusion effects. $\langle S_T \rangle$ values closely correlate with PDFs of Z_f (Fig. 4 (c)).

The trends in $S_{u,ref}$ of laminar flames at increasing H_2-enrichment are in agreement with Z_f correlations shown in Fig. 4 (c), and $S_{u,ref}$ remains closer to S_L^o in the absence of turbulence for the pure hydrocarbon flames. Highly-strained laminar flames are sensitive to thermo-diffusive effects at $Le_{eff} < 1$, where $\mathcal{D}$ is larger than α, which increases local ϕ, and, consequently, temperature and flame velocity increase. Therefore, at constant flame stretch, $S_{u,ref}$ linearly increases and $\langle Z_f \rangle$ linearly decreases at increasing H_2 content for CH_4-H_2-air flames with $Le_{eff} < 1$. However, in C_3H_8-H_2-air flames, the slope appears to change once $Le_{eff} < 1$.

In the counter-flow geometry, laminar flames are stretched mainly due to bulk strain rate: $K_s = dU/dx$, where U is the bulk axial velocity and x is the axial distance. However, in turbulent flames, stretching is due to both bulk strain rate and the stretch effects of turbulent eddies through increasing flamelet curvature (κ). The two components of flame stretch, K_s and $\langle \kappa \rangle$, are illustrated in Figs. 6 (a) and (b).

In general, Figs. 6 (a) and (b) show that the bulk strain rate is larger than the stretch caused by curvature in highly-strained turbulent counter-flow flames. $\langle K_s \rangle$ remains almost constant in laminar and turbulent flames, and is higher in turbulent flames compared to laminar cases. Furthermore, in CH_4-H_2-air flames, $\langle \kappa \rangle S_L^o$ increases with increasing H_2 content, while in C_3H_8-H_2-air flames, $\langle \kappa \rangle S_L^o$ is constant up to 60 % of H_2 content, after which $Le_{eff} < 1$, and $\langle \kappa \rangle S_L^o$ increases sharply. The increase in stretch sensitivity leads to the flame making more frequent incursions to the unburned reactants in mixtures with $Le_{eff} < 1$. Increasing local flamelet curvature also increases the global turbulent burning rates due to an increase in flame surface density [39], which make the flames to burn faster and move further upstream to the high-speed region close to the nozzle, eventually causing flash back in mixtures with high H_2 content.

4. Conclusions

The effects of differential diffusion on laminar and turbulent flame velocities and stabilization of lean premixed flames were investigated in a highly strained counter-flow apparatus. H_2-enriched CH_4-air flames and C_3H_8-air flames, representative of distinct Le_{eff}, were studied at constant laminar flame speeds.

PDFs of instantaneous flame position illustrate that the effects of differential diffusion are only observed in H_2-enriched C_3H_8-air flames when $Le_{eff} < 1$ at H_2 contents of larger than 60 % (by volume), whereas a continuous drop in flame position was observed in H_2-enriched CH_4-air flames, all having $Le_{eff} < 1$, at increasing H_2-enrichment. Furthermore, PDFs of flame position show that the effects of differential diffusion become significant when $Le_{eff} \lesssim 0.8$.

PDFs of local instantaneous apparent turbulent flame velocity closely correlate with the PDFs of flame location. While local turbulent flame velocities are larger in CH_4-H_2-air compared to C_3H_8-H_2-air flames, the PDFs show a slight increase with increasing H_2 content due to the effects of differential diffusion, and have values 2 to 3 times larger than S_L^o.

In highly-strained turbulent counter-flow flames, differential diffusion affects the flame front topology in mixtures with $Le_{eff} < 1$. While bulk strain rates remain nearly constant, we observe a clear increase in curvature when Le_{eff} falls below unity, which then allows the flames to burn faster and propagate further upstream toward the unburned reactants, specifically in mixtures with $Le_{eff} \lesssim 0.8$, eventually leading to flashback.

Acknowledgments

This research was funded by the Natural Sciences and Engineering Research Council of Canada and Siemens Canada Limited under the Collaborative Research and Development program (NSERC-CRD). Support of the McGill Engineering Doctoral Awards (MEDA) program is also gratefully acknowledged.

References

[1] Z. Huang, Y. Zhang, K. Zeng, B. Liu, Q. Wang, D. Jiang, Combustion and Flame 146 (2006) 302–311.
[2] C. Tang, Z. Huang, C. Jin, J. He, J. Wang, X. Wang, H. Miao, International Journal of Hydrogen Energy 33 (2008) 4906–4914.
[3] R. Abdel-Gayed, D. Bradley, M. Hamid, M. Lawes, Proceedings of the Combustion Institute 20 (1984) 505–512.
[4] A. Lipatnikov, J. Chomiak, Progress in Energy and Combustion Science 31 (2005) 1–73.
[5] R. S. Barlow, M. J. Dunn, M. S. Sweeney, S. Hochgreb, Combustion and Flame 159 (2012) 2563–2575.
[6] J. D. Regele, E. Knudsen, H. Pitsch, G. Blanquart, Combustion and Flame 160 (2013) 240–250.
[7] E. Boschek, P. Griebel, P. Jansohn, Proceedings of the ASME Turbo Expo 2007: Turbine Technical Conference and Exposition. GT2007–27496 (2007).
[8] E. Abbasi-Atibeh, S. Jella, J. M. Bergthorson, Proceedings of the ASME Turbo Expo 2018: Turbine Technical Conference and Exposition. GT2018-77139 (2018).
[9] M. Matalon, Combustion Science and Technology 31 (1983) 169–181.
[10] C. Law, Proceedings of the Combustion Institute 22 (1989) 1381–1402.
[11] R. W. Pitz, S. Hu, P. Wang, Progress in Energy and Combustion Science 42 (2014) 1–34.
[12] A. Marshall, J. Lundrigan, P. Venkateswaran, J. Seitzman, T. Lieuwen, Proceedings of the Combustion Institute 35 (2015) 1417–1424.
[13] F. Dinkelacker, B. Manickam, S. Muppala, Combustion and Flame 158 (2011) 1742–1749.
[14] F. Halter, C. Chauveau, I. Gökalp, International Journal of Hydrogen Energy 32 (2007) 2585–2592.
[15] C. Mandilas, M. Ormsby, C. Sheppard, R. Woolley, Proceedings of the Combustion Institute 31 (2007) 1443–1450.
[16] J. F. Driscoll, Progress in Energy and Combustion Science 34 (2008) 91–134.
[17] N. Bouvet, F. Halter, C. Chauveau, Y. Yoon, International Journal of Hydrogen Energy 38 (2013) 5949–5960.
[18] D. Goodwin, Chemical Vapor Deposition XVI and EUROCVD 14 (2003) 2003–08.
[19] G. Coppola, B. Coriton, A. Gomez, Combustion and Flame 156 (2009) 1834–1843.
[20] E. Mastorakos, A. Taylor, J. Whitelaw, Combustion and Flame 102 (1995) 101–114.
[21] D. Geyer, A. Kempf, A. Dreizler, J. Janicka, Combustion and Flame 143 (2005) 524–548.
[22] F. Hampp, R. Lindstedt, Combustion and Flame 182 (2017) 248–268.
[23] E. Mastorakos, A. Taylor, J. Whitelaw, Combustion and flame 91 (1992) 40–54.
[24] K. Sardi, A. Taylor, J. Whitelaw, Journal of Fluid Mechanics 361 (1998) 1–24.
[25] A. Kempf, H. Forkel, J.-Y. Chen, A. Sadiki, J. Janicka, Proceedings of the Combustion Institute 28 (2000) 35–40.
[26] G. Coppola, A. Gomez, Experimental Thermal and Fluid Science 33 (2009) 1037–1048.
[27] R. Borghi, in: Recent Advances in the Aerospace Sciences, Springer, 1985, pp. 117–138.
[28] B. Böhm, O. Stein, A. Kempf, A. Dreizler, Flow, Turbulence and Combustion 85 (2010) 73–93.
[29] H. Tennekes, J. Lumley, A First Course in Turbulence, The MIT Press, Cambridge, USA, 1972.
[30] J. Hinze, New York 218 (1975).
[31] N. Peters, Turbulent combustion, Cambridge university press, 2000.
[32] S. A. Filatyev, J. F. Driscoll, C. D. Carter, J. M. Donbar, Combustion and Flame 141 (2005) 1–21.
[33] S. Kheirkhah, Ö. L. Gülder, Combustion and Flame 162 (2015) 1422–1439.
[34] H. Kolla, J. Rogerson, N. Swaminathan, Combustion Science and Technology 182 (2010) 284–308.
[35] P. J. Trunk, I. Boxx, C. Heeger, W. Meier, B. Böhm, A. Dreizler, Proceedings of the combustion institute 34 (2013) 3565–3572.
[36] G. Hartung, J. Hult, R. Balachandran, M. Mackley, C. Kaminski, Applied physics B 96 (2009) 843–862.
[37] R. Abu-Gharbieh, G. Hamarneh, T. Gustavsson, C. F. Kaminski, Optics Express 8 (2001) 278–287.
[38] I. R. Gran, T. Echekki, J. H. Chen, Proceedings of the combustion institute 26 (1996) 323–329.
[39] J. Hult, S. Gashi, N. Chakraborty, M. Klein, K. W. Jenkins, S. Cant, C. F. Kaminski, Proceedings of the Combustion Institute 31 (2007) 1319–1326.